Progress in Organic Coatings 216 (2026) 110190

Contents lists available at ScienceDirect

Progress in Organic Coatings

journal homepage: www.elsevier.com/locate/porgcoat

Anisotropy control of GO-CNC nanofillers in chitosan-based ultrasonic-sprayed nanocomposite coatings to improve oxygen and water vapor barrier properties of PBS films

Alessia Cabrini [a], Hanieh Kargarzadeh [b], Giovanna Giuliana Buonocore [c], Artur Różański [b], Luigi De Nardo [d], Gennaro Gentile [e], Pierfrancesco Cerruti [a,e,*], Marino Lavorgna [a,c]

[a] Institute of Polymers, Composites and Biomaterials, National Research Council of Italy, via Previati 1/E, 23900, Lecco, Italy
[b] Center of Molecular and Macromolecular Studies, Polish Academy of Sciences, Sienkiewicza 112, 90-363, Lodz, Poland
[c] Institute of Polymers, Composites and Biomaterials, National Research Council of Italy, P.le Fermi, 1, 80055, Portici, Naples, Italy
[d] Department of Chemistry, Materials and Chemical Engineering "G. Natta", Politecnico di Milano, Milano, Italy
[e] Institute for Polymers, Composites and Biomaterials, National Research Council of Italy, via Campi Flegrei, 34, 80078, Pozzuoli, Naples, Italy

ARTICLE INFO

Keywords:
Chitosan
Nanocrystalline cellulose
Graphene oxide
Nanocomposite coatings
Oxygen barrier properties
Water vapor barrier properties

ABSTRACT

This study compares two sustainable polymer-based nanocomposite coating architectures: a single-layer coating composed of chitosan (CH), graphene oxide (GO), and cellulose nanocrystals (CNC), cross-linked with borax (B), and a bilayer system in which an outer layer containing GO and borax-crosslinked CNC is applied onto a borate-crosslinked CH matrix incorporating GO. The two systems were designed to highlight the effect of the spatial segregation of the fillers in improving the oxygen and water vapor barrier performance of polybutylene succinate (PBS) films, evaluating an isotropic or anisotropic distribution of fillers across the coating thickness, while maintaining a bio-based and environmentally friendly material platform. Swelling tests confirmed that borax effectively crosslinks the nanocomposite material comprised of both GO and CNC, significantly enhancing the water swelling resistance of the coating formulations. Morphological analysis revealed compact, defect-free structures with uniform nanofiller dispersion and orientation in the nanocomposite single-layer, while the biayer system exhibited a highly aligned GO in the bottom layer and a compacted filler network in the upper layer. Gas barrier test showed that oxygen permeability was reduced by up to three orders of magnitude at 5% RH and by one order at 50% RH, compared to uncoated PBS. Water vapor permeability (WVP) was also improved, particularly in the bilayer coating, where WVP decreased by 25%. These findings highlight the effectiveness of tailored nanofiller distribution and hybrid filler generation in developing high oxygen and water barrier sustainable coatings, suitable for oxygen-sensitive packaging in humid environments.

1. Introduction

Polymeric barrier materials are employed in a wide range of applications, including food and pharmaceutical packaging as well as electronics (e.g., flexible devices, OLEDs, solar cells) [1,2]. Conventional high-performance solutions often rely on multilayer polymer systems or monolayer films coated with inorganic thin layers, such as metal and metal oxide, which provide excellent gas and moisture barrier [3,4]. Despite their efficiency, these structures pose serious environmental challenges: multilayers are difficult to separate and recycle, while inorganic coatings compromise the biodegradability of otherwise compostable films. As a result, there is increasing demand for barrier materials that not only deliver high performance but are also bio-based and biodegradable, with sustainable end-of-life options [5]. Biomaterials, such as chitosan and cellulose derivatives, have attracted growing attention as candidates for sustainable barrier materials due to their abundance, renewability, biodegradability, and biocompatibility [6]. Both materials are capable of forming dense networks with inherently low oxygen permeability, making them promising alternatives to synthetic polymers in packaging applications. However, their strong hydrophilic character leads to excessive swelling and moisture sensitivity, resulting in poor water resistance and compromised barrier performance under humid conditions [7]. These limitations have so far restricted their industrial use, especially in the packaging of oxygen- and

* Corresponding author at: Institute of Polymers, Composites and Biomaterials, National Research Council of Italy, via Previati 1/E, 23900, Lecco, Italy.
E-mail address: pierfrancesco.cerruti@cnr.it (P. Cerruti).

https://doi.org/10.1016/j.porgcoat.2026.110190
Received 22 January 2026; Received in revised form 27 March 2026; Accepted 13 April 2026
Available online 18 April 2026

moisture-sensitive products. Considerable research has therefore been devoted to enhancing the mechanical strength and barrier efficiency of chitosan- and cellulose-based films, aiming to bridge the gap with conventional polymers [8].

One promising strategy to overcome these drawbacks is the incorporation of high-aspect-ratio nanofillers into polysaccharide matrices, which can create more tortuous diffusion pathways for permeating molecules [9]. In a previous study, chitosan (CH)/graphene oxide (GO) nanocomposite coatings deposited by ultrasonic spraying coating (USS) technology have been shown to significantly enhance the gas barrier of polybutylene succinate (PBS) films [10]. However, due to the hydrophilicity of both chitosan and GO, these coatings still performed poorly under high humidity and did not improve water vapor resistance. This highlights the need to explore the interaction of two nanofillers in the same system, combining, for example, one-dimensional nanocellulose with two-dimensional graphene oxide, to reduce water sensitivity while maintaining or enhancing gas barrier properties.

Cellulose nanocrystals (CNC), obtained from cellulosic biomass, are stiff, rod-like, and high-aspect-ratio nanomaterials (5–10 nm wide, 100–200 nm long), capable of forming a wide interface with the polymer matrices [11]. This makes them attractive candidates for producing bionanocomposite materials with enhanced mechanical, gas barrier, and water barrier properties [12]. Due to the two materials' compatibility, CNCs have been used as a reinforcement for chitosan to fabricate eco-friendly nanocomposite materials [13,14], with studies reporting a progressive reduction in water absorption and water vapor permeability (WVP) with an increase in CNCs content [15]. However, it has also been shown that WVP increases beyond a certain CNCs concentration (approximately 6–8% by weight), due to the CNCs' tendency to self-associate and aggregate during nanocomposite preparation [16,17]. Hybrid nanofillers combining CNCs with graphene oxide (GO) have been proposed as a way to overcome such limitations. El Miri et al. demonstrated that combining CNCs and GO in a hybrid nanofiller (i.e., a filler composed of two kinds of nanoparticles with different shapes) promotes a more homogeneous dispersion in a poly(vinyl alcohol) (PVA) matrix, thanks to the hydrogen bonding interactions generated between the hydroxyl and oxygen-containing groups on the surface of both nanomaterials [18]. Similarly, Santillo et al. showed that adding GO and CNCs together to chitosan films improved filler distribution and yielded better mechanical and water barrier properties than pristine chitosan [19]. These results suggest that GO–CNCs synergy is a promising route to suppress nanofiller aggregation while maximizing barrier performance.

Building on this knowledge, the present work develops two novel coating architectures by exploiting the GO-CNC hybrid filler concept and tailoring nanofiller distribution to realize either an isotropic or directional (anisotropic) filler distribution throughout the coating thickness. In the first approach, a homogeneous CH/GO/CNC nanocomposite coating is designed, with borax (B) as a crosslinker to bind CH chains with GO sheets and CNC rods. Borax has been reported to form strong crosslinking networks with hydroxyl-rich polymers and nanomaterials such as cellulose nanofibers (CNF) [20], PVA [21], CH [22], and GO, yielding denser and less hydrophilic structures. For instance, Lai et al. used borax to generate a bio-inspired crosslinked PVA/GO network that significantly improved the oxygen barrier performance by increasing the effective aspect ratio of GO sheets [21].

The second approach is inspired by the"nanobrick wall" structure. In this strategy, cellulose nanomaterials are combined with impermeable 2D nanomaterials (e.g., clays, carbon-based nanomaterials) to form a layered architecture that enhances barrier properties [23]. For example, F. Ren et al. enhanced the barrier properties of CNF films by incorporating GO and promoting nanoplatelet alignment. The highly oriented CNF/GO nanocomposite films exhibited outstanding oxygen barrier properties and good water vapor barrier performance [24]. Based on this concept, the present study developed a bilayer coating composed of a CH/GO layer beneath an upper layer of CNC and GO. Both layers were cross-linked with borax to create a denser, less hydrophilic material. In the top layer, CNC and GO form a compact filler network with highly aligned nanoplatelets and nanofibrils, resulting in a strongly anisotropic distribution throughout the coating thickness.

The novelty of this work lies in the comparison between coating architectures featuring an isotropic nanofiller distribution throughout coating thickness and an anisotropic configuration in which the fillers are organized into two distinct layers, decoupling the oxygen and water vapor barrier mechanisms. So far, no study has reported the integration of CNC–GO hybrid fillers with borax crosslinking in chitosan to coat compostable PBS films, nor their direct comparison under varying relative humidity conditions. While previous studies have focused on either CNC–GO synergy or borax crosslinking separately, this work demonstrates their combined effect on gas and water barrier performance.

2. Experimental

2.1. Materials

Medium molecular weight chitosan (CH) powder (degree of deacetylation ≥75%, molecular weight 190–310 kDa according to supplier specifications), sodium tetraborate decahydrate (borax, 99%), and acetic acid were purchased from Sigma-Aldrich. Graphene oxide (GO) nanosheets were synthesized from graphite flakes (Qingdao Dahe Graphite Co. Ltd., China) using the Hummers method [25]. A thixotropic gel of CNCs (concentration: 3 wt%, sulfur content: 91 mmol kg^{-1}, zeta potential: −28.5 mV) was obtained from cellulose pulp via sulfuric acid hydrolysis [26] and kindly supplied by Melodea Ltd. (Rehovot, Israel). Flexible 30-μm-thick polybutylene succinate (PBS) films, supplied by Corapack (Como, Italy), were used as coating substrates.

2.2. Preparation of coating solutions

2.2.1. Graphene oxide/nanocellulose/chitosan hybrid isotropic coatings

A GO suspension (0.1 wt%) was prepared in deionized (DI) water and homogenized by ultrasonication for 2 h with a tip sonicator (FB-505, Fisherbrand). The CNCs' thixotropic gel was diluted to 2 wt% with DI water, stirred for 30 min, and then sonicated for 5 min to obtain a homogeneous CNCs dispersion. The CH solution (1 wt%) was prepared by adding CH powder to a 1% *v*/v acetic acid solution (pH = 2.5) and stirred for 24 h at room temperature. The nanocomposite mixture was prepared by adding the GO and CNCs dispersions into the CH solution under vigorous stirring, followed by sonication for 10 min with the tip sonicator. The added amount of nanofiller dispersions corresponds to a final concentration of GO and CNC equal to 1.0 wt% and 5.0 wt%, respectively, based on the CH weight. Then, borax (B) was pre-dissolved in DI water (~0.5 ml), added to the mixture, and stirred for 1 h; the borax concentration was 10 wt%, corresponding to 1.0 wt% of boron element based on CH weight. A schematic of the resulting coating material, coded CH/B/GO/CNC, is reported in Fig. 1. To highlight the effect of CNCs, the coating formulation was also prepared as described above, but using only GO as filler (coded CH/B/GO).

2.2.2. Chitosan/graphene oxide and Nanocellulose/graphene oxide bilayer anisotropic coatings

The bilayer anisotropic coatings were obtained by first preparing the CH/B/GO mixture and depositing it as a bottom layer. Following the procedure reported in the previous section, 1 wt% of GO and 10 wt% of borax relative to CH weight were added to the CH solution. The second layer, consisting primarily of CNCs, was deposited after the complete solvent evaporation of the previous layer. The second layer formulation was prepared by adding GO dispersion into the 1.5 wt% CNCs dispersion to reach a GO content of 3 wt% based on the amount of CNCs. The GO/CNC filler dispersion was homogenized by 30 min of tip sonication. Subsequently, borax was pre-dissolved into DI water (~ 0.5 ml), added

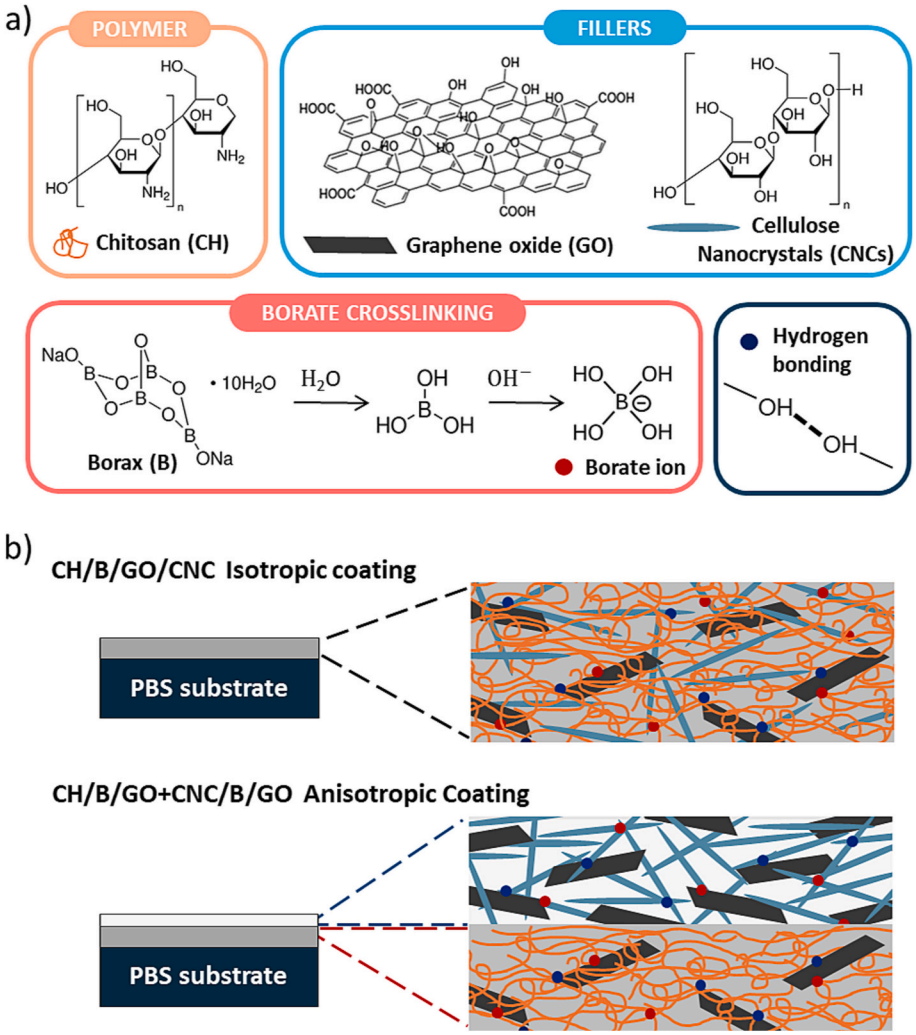

Fig. 1. Chemical structures of the materials (a) and schematic illustration of the coatings with isotropic and anisotropic filler distribution (b).

to the GO/CNC dispersion, and stirred for 1 h. The amount of borax added was 10 wt%, corresponding to 1.0 wt% of boron element based on the CNCs' weight. Before the deposition step, the pH of the solution was adjusted from 8 to 11 by adding 0.15% *v*/v of 1.5 M NaOH to favor the formation of borate ions from borax hydrolysis. Fig. 1 illustrates the configuration of the resulting anisotropic coating, coded CH/B/GO+CNC/B/GO. For comparison, bilayer coatings were prepared as described above but using only the CNCs dispersion or the CNC/B mixture to deposit the second layer, coded CH/B/GO+CNC and CH/B/GO+CNC/B, respectively.

2.3. Coating realization

The coating mixtures were deposited onto PBS films using a SimCoat Ultrasonic Spray Coater (SONO-TEK), equipped with an Impact nozzle. Before coating, the PBS film was rinsed with distilled water and ethanol, then plasma-treated using plasma surface technology (Diener Pico) in air, for 10 min at 90 μA and 0.4 mbar. The conditions applied for the deposition of the different coating layers, in terms of USS process parameters and solution characteristics, are reported in Tables S1 and S2. Each deposited layer was dried at room temperature under a hood for 15 min before depositing the successive layer. Lastly, all the coated PBS films were dried in a fan oven at 70 °C for 50 min to remove water and promote the borax-crosslinking reaction.

2.4. Characterization methods

Fourier-transform infrared (FTIR) spectra of free-standing CH- and CNC-based films were recorded in attenuated total reflection (ATR) mode using an FTIR spectrometer (Nicolet iS 10, Thermo Fisher Scientific, Waltham, MA) at room temperature. Infrared spectra were recorded from 500 to 4000 cm^{-1}, performing 32 scans at 1 cm^{-1} resolution. For each formulation, two film specimens were analyzed, and two spectra were acquired for each film.

Water swelling tests evaluated water stability. Four circular specimens for each film type were weighed and immersed in Petri dishes filled with phosphate-buffered saline (PBS; NaCl 120 mM, KCl 2.7 mM, Na_2HPO_4 10 mM, pH 7.4). At selected time intervals (1, 2, 3, 6, 24, and 48 h), the specimens were removed, gently blotted to eliminate excess surface liquid, weighed, and subsequently re-immersed in Petri dishes containing fresh solution. The percentage of swelling ratio (SR) was calculated according to Eq. (1).

$$SR\ (\%) = \frac{w_t - w_0}{w_0} \times 100 \quad (1)$$

where w_t is the mass of the swollen sample at different time points, and w_0 is the initial mass of the sample.

The morphological analysis was conducted on an FEI Quanta 200 FEG Scanning Electron Microscope (SEM) (FEI, Eindhoven, Netherlands) at an acceleration voltage of 5–10 kV. Before the

observation, the specimens were cryogenically fractured in liquid nitrogen, and their surface was sputter-coated with Au—Pd alloy to make them conductive, using a BalTec MED020 unit. Surface and cross-sectional images were acquired; the latter were analyzed using ImageJ software to calculate the coating thickness. Transmission electron microscope (TEM) images were obtained with Tesla BS 500 (Tesla, Czech Republic) operating at an accelerating voltage of 90 kV. For TEM analysis, ultra-thin slices approximately 60 nm thick were prepared by cryo-ultramicrotomy at −40 °C using an ultramicrotome (PowerTome PC, Boeckeler, USA) equipped with a 35° diamond knife (Diatome, Switzerland). The sections were mounted on standard copper grids. Before imaging, no staining or additional chemical treatments were applied.

Oxygen transmission rate (OTR) was tested using an Oxtran 2/21 ML instrument (AMETEK MOCON Inc., Minneapolis, MN), at 23 °C under 5% or 50% RH, in accordance with ASTM D3985 for 0% RH and ASTM F1927 for 50% RH. The measurements were carried out in triplicate. The coated film's oxygen permeability (OP) was calculated from OTR data, using Eq. (2).

$$OP = OTR\ \frac{h}{\Delta p} \tag{2}$$

Where h is the thickness of the coated film and Δp the difference of relative humidity across the films. The coating permeability P_c was mathematically decoupled from the substrate P_s utilizing the ideal laminate theory:

$$P_{ILT} = \left(\frac{\varphi_s}{P_s} + \frac{\varphi_c}{P_c}\right)^{-1} ; \varphi_{i=c,s} = d_{i=c,s} \Big/ d \tag{3}$$

where P_{ILT} is permeability of a coated film, d_s and φ_s are the thickness and volume fraction of the polymer substrate, while and d_c and φ_c and are the thickness and volume fraction of the coating layer. Since the permeability of the uncoated PBS substrate and that of the coated films were measured on independent specimens, no direct pairing between individual replicates could be established. Therefore, the coating permeability was calculated for each coated-film replicate using the mean permeability of the uncoated PBS substrate within the ideal laminate model.

The water vapor transmission rate (WVTR) was evaluated using the dry cup method, according to the ASTM E96-22 standard. The permeation cups (VF2201, TQC sheen, The Netherlands), with a diameter of 25 cm^2, were filled with dry calcium chloride as a desiccant to achieve an internal 0% relative humidity (RH). Subsequently, the coated PBS films were sealed on the permeation cups, and the cups were stored at 100% RH and 25 °C. Three specimens were tested for each type of coating. Weight measurements were regularly acquired at stationary conditions and the slope (W) of the weight gain vs time curves was determined by linear regression. The WVTR was then calculated using Eq. (3):

$$WVTR = \frac{W}{A}\ \left[\frac{g}{m^2\ d}\right] \tag{3}$$

where A is the permeation area of the cups [m^2], and W is the slope of weight gain against time [g d^{-1}]. As the samples have different thicknesses, the comparison was made on water vapor permeability (WVP). The WVP was calculated using the Eq. (4):

$$WVP = \frac{WVTR}{\Delta p\ P^0_{H_2O}}\ h \tag{4}$$

where $P^0_{H_2O}$ is the water saturation pressure.

Permeability tests were carried out in triplicate, and the results are expressed as mean ± standard deviation. Statistical analysis was performed using Python with the statsmodels and SciPy libraries. Comparisons among groups were conducted using one-way ANOVA followed by Tukey's post hoc test, with a significance level of $\alpha = 0.05$. Statistically significant differences ($p < 0.05$) are indicated in the charts using letters.

3. Results and discussion

3.1. Study of coating formulation

To optimize the properties of the hybrid isotropic and bilayer anisotropic coatings, a series of CH- and CNC-based water suspensions, summarized in Table 1, were prepared to obtain free-standing films via solvent casting. The water suspensions were first characterized to assess their zeta potential absolute values, to reveal distinct surface charges and interactions in the coating suspensions. CNC suspension (−36.7 mV) and borax solution (−20.8 mV) both carry negative charges typical of their hydroxyl/carboxyl groups, while GO (−28.8 mV) showed stronger anionic character. Chitosan (CH, +45.7 mV) was the sole cationic component in the formulations, and it maintained high positive charge even after borax addition (46.3 mV), indicating borate crosslinking occurs without neutralizing CH amino groups. Addition of GO did not change the potential, while the presence of CNC in ternary and quaternary systems caused the potential to slightly decrease to about +39 mV, suggesting the formation of stable polyelectrolyte complex with partial charge neutralization because chitosan is still in excess. It is likely that borax favor interaction between CH and CNC via hydroxyl reaction, while GO could establish electrostatic and H-bonding interactions with CH. Regarding the CNC-based coating formulations, CNC/GO showed an absolute value (−31.7 mV) in between those of CNC and GO, indicating stable co-dispersion without flocculation. Both anionic nanofillers likely form H-bond networks between surface hydroxyls (-OH on CNC) and GO carboxyl/epoxy groups, enhancing colloidal stability. No charge neutralization occurs, preventing aggregation. The addition of borax contributes to a decrease in absolute value of potential, likely due to a charge screening effect on hydroxyl groups.

Films were analyzed to evaluate the variation of chemical structure and water stability due to the borax crosslinking and GO or CNC addition. When borax is dissolved in water, it hydrolyzes, yielding boric acid $B(OH)_3$ and tetrahydroxyborate $B(OH)_4^-$; boric acid exists in equilibrium with the borate anions (Eq. (5)):

$$B(OH)_3 + OH^- \leftrightharpoons B(OH)_4^- \tag{5}$$

Table 1
Composition and zeta potential of CH-based and CNC-based suspensions, used to prepare free-standing films. a) Borax, GO, and CNC contents are reported based on CH or CNC weight as matrix.

Code	CH/CNC concentration (as matrix)	Borax content [a)]	GO content [a)]	CNC content [a)]	Zeta Potential (mV)
CH	1.0 wt%	–	–	–	45.7 ± 7.6
CH/B	1.0 wt%	10 wt%	–	–	46.3 ± 2.0
CH/B/GO	1.0 wt%	10 wt%	1 wt%	–	47.0 ± 1.2
CH/GO/CNC	1.0 wt%	–	1 wt%	5 wt%	39.3 ± 3.2
CH/B/GO/CNC	1.0 wt%	10 wt%	1 wt%	5 wt%	39.4 ± 2.3
CNC	1.5 wt%	–	–	–	−36.7 ± 0.4
CNC/B	1.5 wt%	10 wt%	–	–	−30.0 ± 2.3
CNC/GO	1.5 wt%	–	3 wt%	–	−31.7 ± 1.0
CNC/B/GO	1.5 wt%	10 wt%	3 wt%	–	−25.7 ± 1.2

The predominance of either boric acid or borate anions may strongly influence the structure and properties of borax-crosslinked polymers [27]. Borate anions easily react with hydroxyl groups via diol complexation by either covalent or hydrogen bonding [28]. In contrast, boric acid preferably reacts with carboxyl and amine groups [29]. The crosslinking generated by tetrahydroborate ion reaction with hydroxyl groups in CH molecules and CNC nanofibers, or carboxyl groups and hydroxyl groups in GO nanosheets, is promoted by temperature and pH increase [21–30]. For this reason, the pH of the CNC-based coating formulations was adjusted to 11 by adding NaOH. Since CH is soluble only in acidic environments, after deposition and drying, chitosan-based coatings were heat- treated at 70 °C, which is the maximum temperature to avoid modifying the mechanical characteristics of the PBS substrate. The effect of borax crosslinking on the structure of CH- or CNC-based nanocomposites was assessed through ATR-FTIR analysis, and its effect on their water stability through swelling tests.

The FTIR spectra of pristine CH-based nanocomposites are shown in Fig. 2a. Also, Fig. S1 in SI reports the difference FTIR spectra, which help to better visualize the spectral variations in band intensity and position associated with borate crosslinking, and the interactions of CH with GO and CNC. The spectrum of CH shows the typical broad band in the 3600 to 3000 cm^{-1} range due to -OH and -NH stretching, with two peaks at 3360 and 3289 cm^{-1}, and the absorption bands of amide groups at 1650 cm^{-1} and 1560 cm^{-1}, ascribed to the C═O stretching and N—H bending modes (amide II), respectively. The peak at 1410 cm^{-1} is related to the N—H deformation vibration of amide (amide III), and peaks at 1380 cm^{-1} and 1324 cm^{-1} are ascribed to the methylene and C-O-H stretching of a primary alcoholic group, respectively. Furthermore, the absorption bands of C—O at 1156 cm^{-1} correspond to the anti-symmetric stretching of the C-O-C bridge, and the band at 1070 cm^{-1} was assigned to the secondary hydroxyl group [31]. The FTIR spectra of CH/B films exhibit a decrease of the -OH/-NH band, and a reduction of peak intensity at 1070 cm^{-1} compared to that at 1032 cm^{-1} [32]. The occurrence of this variation in the spectrum following the addition of borax as crosslinking agent indicates an interaction between borate ions and hydroxyl moieties, with a consequent decrease in the -C-OH bond presence. The intensity variation of the two bands is also observed by comparing CH/GO/CNC and CH/B/GO/CNC spectra, although to a lower extent, likely due to the presence of a higher number of hydroxyl groups in the system at the same borax content. These results indicate that borax generates a cross-linked network that connects CH and the nanofillers, due to its interaction with either GO or CNC hydroxyl groups. Additionally, spectra of films containing borate show a reduction in the intensities of the amide II and amide III peaks, likely due to the molecular interactions between boric acid and chitosan. The peak at 1326 cm^{-1} significantly increases in intensity and slightly shifts toward higher wavelengths because of the overlap with the band related to the asymmetric stretching vibration of B-O-C bonds, located at 1336 cm^{-1} [33]. FTIR results indicate the occurrence of the reaction of borax with the functional groups of both CH, CNC and GO nanofillers, which confirms the formation of a borax cross-linked network linking CH with the fillers.

The FTIR spectra of CNC-based films are shown in Fig. 2b. All the samples display adsorption peaks of cellulose I [34]. The band at 3345 cm^{-1} corresponds to the characteristic –OH stretching vibration from intra- and intermolecular hydrogen-bonded hydroxyl groups. The band at 2901 cm^{-1} is assigned to aliphatic saturated CH–CH stretching in the glucose units. Other peaks detected include 1640 cm-1, 1430 cm-1, and 1164 cm-1, attributed to water absorbed onto cellulose, the CH2 symmetrical bending, and the asymmetrical C–O–C bridge stretching from the glycosidic bond. The band at 1060 cm-1 represents C—O stretching vibration, and the peak at 898 cm-1 is typical of asymmetric out-of-plane ring stretching. The incorporation of 3 wt% of GO does not provide any clear differences in the FTIR spectra, due to the overlapping of GO characteristic peaks with those of CNC [35]. As observed in the spectra of chitosan films, the introduction of borax causes the decrease of the peak associated with –OH stretching, due to the reaction of hydroxyl groups of CNC with borate ions. Also, new peaks appear at 1570 cm-1, related to the asymmetric stretching vibration of B-O-C bonds, and the peak at 886 cm-1, derived from B—O stretching vibration from residual borate [36].

During the preparation of CNC/B and CNC/B/GO coating mixtures, the mixture pH was increased to 11 to generate a larger amount of borate ions, thereby favoring their crosslinking reaction with CNC or GO. Borate ions, which are mainly present at pH above the boric acid pK_a of 9.2 [37], can form a covalent crosslinking network with hydroxyl groups of cellulose, or, otherwise, physical crosslinking through hydrogen bonding could be formed between the ring structures of the cellulose chain and borax [38]. From the FTIR results, it is difficult to assess whether chemical or physical crosslinks were mainly formed in the system. However, as previously reported for other cellulose nanomaterials (e.g., CNF), the nanocellulose-borax crosslinking reaction in alkali conditions involves the formation of a bis-chelate cellulose-OH−B−OH-cellulose complex of the borate anion with the C2,3-diol on the CNC [20–33].

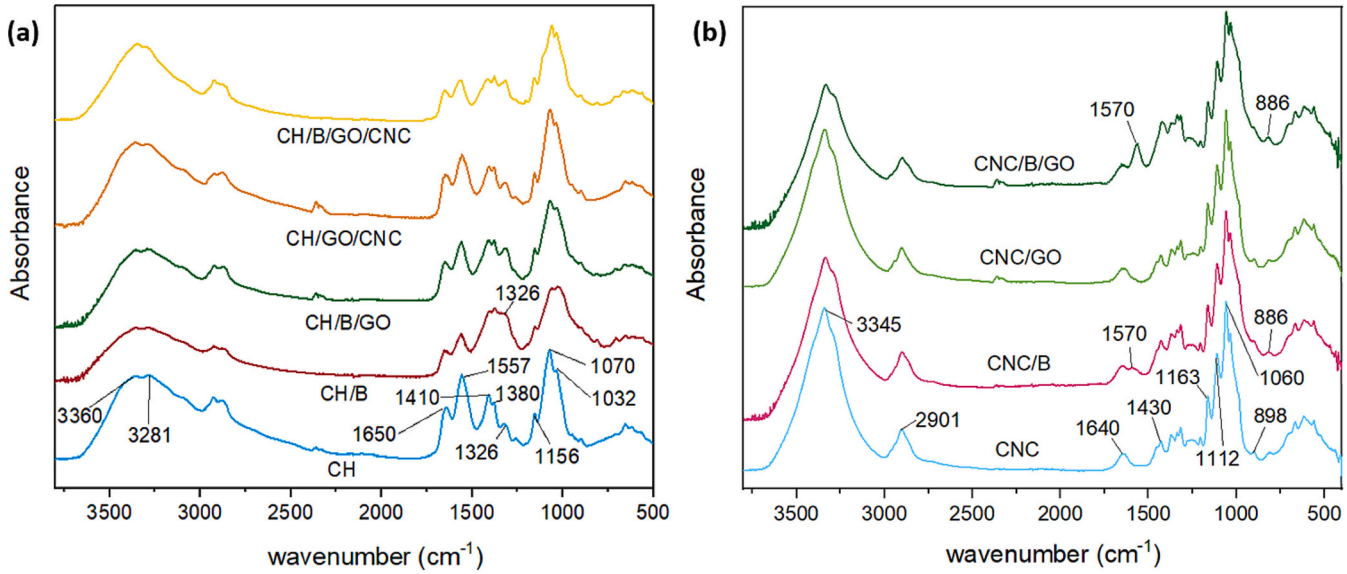

Fig. 2. FTIR spectra CH-based (a) and CNC-based (b) composite formulations after normalization (reference peaks at 1032 cm^{-1} for (a) and 1069 cm^{-1} for (b)).

Fig. 3 shows the swelling dynamics of the prepared films over two days at pH 7.4 and room temperature. The swelling value of pristine CNC, after attaining a maximum weight gain of about 300% in 2 h of immersion, slowly decreases, likely due to the breaking of hydrogen bonds formed between adjacent cellulose chains and the progressive CNC film dissolution. Conversely, CNC/B and CNC/B/GO swelling values increase significantly in the first 2 h of immersion, then slowly increase toward swelling equilibrium (SW ≈ 300% and 270%, respectively). In the initial swelling phase, a high-water uptake and network expansion occur due to the breaking of hydrogen bonds that form between CNC chains or CNC and GO nanosheets in the non-crosslinked regions [24]. At the same time, the covalent crosslinks generated by borate ions between CNC chains, or between CNC and GO, limit further network expansion and water absorption [39]. The introduction of GO to the borax-crosslinked CNC reduces water uptake, likely due to the increase of crosslinking bonds and water-impermeable regions. It should be noted that CH quickly achieves a high weight gain - approximately 1200% in 6 h of soaking (Fig. S2). CH films dissolved after 24 h, so further measurements were not possible; this might be attributed to residual acetic acid. Crosslinking CH with 10 wt% borax results in a drastic reduction of weight gain during the swelling test, reaching a constant equilibrium value of approximately 186%. The water uptake reduction is attributed to the developed covalent crosslinked network involving reactive CH hydrophilic groups such as amine and hydroxyl groups. However, the addition of GO alone increases water absorption, due to the increment of hydroxyl or oxygen-containing groups not involved in the cross-linked network and able to interact with water molecules [40]. Instead, the borax-crosslinked CH films reinforced with both fillers perform better than those crosslinked only. This effect might be attributed to better filler dispersion, which promotes their covalent crosslinking with CH chains [41,42]. Thus, the simultaneous incorporation of the two nanofillers in the CH/B films significantly reduces their water absorption and moisture sensitivity.

In summary, borax cross-linking improves water swelling resistance by developing a tight structure that prevents network swelling. Also, the combination of CNC and GO shows a beneficial effect in improving the coating formulation's water resistance.

3.2. Optimization of the deposition process

Ultrasonic spray coating was used to coat plasma-activated PBS films since this technique allows for a fast and precise deposition of highly homogeneous and thin coating layers. Nevertheless, the efficacy of deposition depends on several material and process parameters that strongly influence the uniformity of the coating material distribution [43]. In a previous study, the optimal parameter combination was suitably investigated through several screening tests, using a 1 wt% chitosan solution as reference [10]. Thus, the optimized process parameters (Table S1) were also used in this study to deposit CH/B/GO/CNC hybrid isotropic coating and CH/B/GO bottom layer of bilayer anisotropic coatings. However, the CNC-based coating mixtures for the upper layer exhibited a markedly different apparent viscosity compared to the chitosan solution. Since this characteristic strongly affects the parameter setting process, the deposition parameters were re-optimized following the guidelines indicated in the previous study and using a 1.5 wt% CNCs dispersion as a reference. The parameters and selected values studied are reported in Table S2. Both coatings were prepared by depositing overlapping layers (comprising 4 deposition cycles of the spray nozzle) with intermediate drying steps, using the minimum amount of sprayed solution for each layer to achieve complete microdroplet coalescence and a continuous liquid layer. This approach allows for a more homogeneous material distribution, avoiding the so-called “ring-coffee” effect, which leads to the accumulation of nanocomposite material in specific areas of the film during solvent evaporation [44].

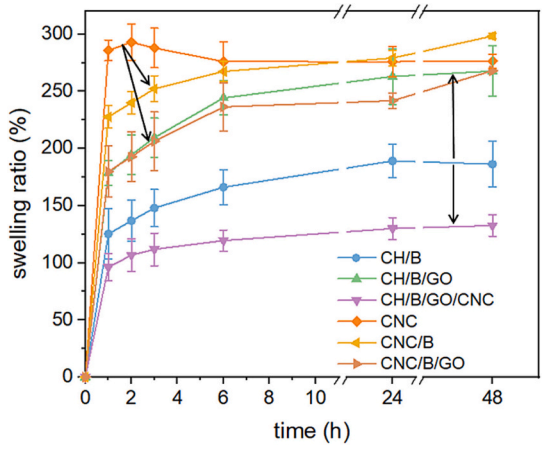

Fig. 3. Swelling profiles of CNC, CNC-based, and CH-based composite formulations in PBS buffer solution (pH 7.4). Arrows highlight the borax-crosslinking effect on CNC-based formulation (top-left), and the effect of CNC and GO incorporation on CH-based formulation.

3.3. Morphological characterization

Scanning electron microscopy (SEM) analysis was carried out on surfaces (Fig. 4) and cross-sections (Fig. 5) of CH/B/GO, CH/B/GO/CNC, and CH/B/GO+CNC/B/GO coatings. SEM examination of the film surface (Fig. 4a and c) reveals changes in coating morphology after deposition of the second layer on the CH/B/GO first layer and the high coverage of the second layer. CH/B/GO/CNC hybrid nanocomposite monolayer (Fig. 4b) and CH/B/GO+CNC/B/GO bilayer (Fig. 4c) coatings exhibit a compact, rougher surface without holes or defects. The rougher morphology observed in the monolayer sample containing CNC is primarily due to the high loading of high aspect ratio fillers and local heterogeneous dispersion [22,45], which hinder polymer chain rearrangement during solvent evaporation, promoting the formation of heterogeneous filler microdomains on the film surface [46,47]. Borax crosslinking may facilitate the filler aggregation by forming a three-dimensional network via borate ions interacting with chitosan functional groups, reducing chain mobility. In CH/B/GO+CNC/B/GO, the absence of chitosan in the upper layer further enhances the surface roughness due to filler dispersion heterogeneity.

However, it is important to note that cross-section images display compact structures without any visible porosity or cracks for all the studied coatings, indicating good compatibility and interaction between the deposited layers. This evidence is even more significant for the bilayer anisotropic coatings, suggesting that electrostatic or hydrogen interactions were attained between the CNC-based upper and CH-based bottom layers. For the bilayer coatings with the upper layer consisting of CNCs or CNC/B/GO (Fig. 5b and c), it is possible to notice a change in the contrast and the morphology along the cross-section attributable to the layer interface (indicated by arrows). These coatings exhibit average thicknesses of 2.33 ± 0.06 μm and 2.21 ± 0.09 μm, respectively, comprising a 1.6 μm-thick CH/B/GO bottom layer and thinner CNC or CNC/B/GO top layers. Also, the thickness of the CH/B/GO/CNC nanocomposite monolayer is around 1.6 μm (Fig. 5c). Hence, the thickness is roughly that of CH/B/GO coatings containing the same amount of GO and prepared with the same deposition method, parameters, and number of spraying cycles (8 cycles with an intermediate drying phase) [10]. Therefore, the simultaneous incorporation of 1 wt% GO and 5 wt% CNCs does not affect the thickness of crosslinked CH coatings, which is typically associated with a good level of nanofiller dispersion [21], while the presence of nanofiller stacks generally leads to an increase in coating thickness [48].

TEM analysis of the CH/B/GO+CNC/B/GO coating was performed to better visualize this morphology variation (Fig. 6a, b and c). By TEM

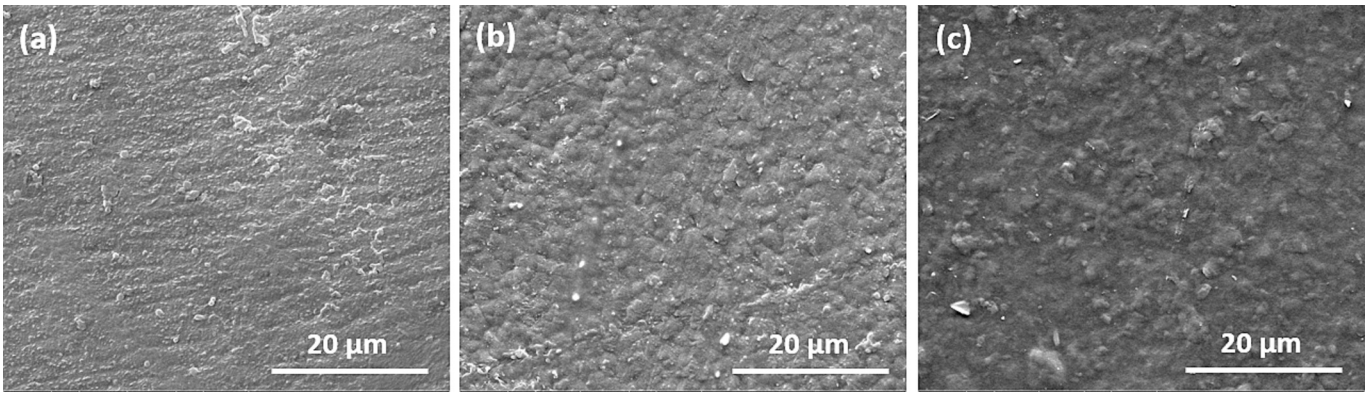

Fig. 4. SEM surface images of CH/B/GO (a), CH/B/GO/CNC (b), and CH/B/GO+CNC/B/GO (c) coatings.

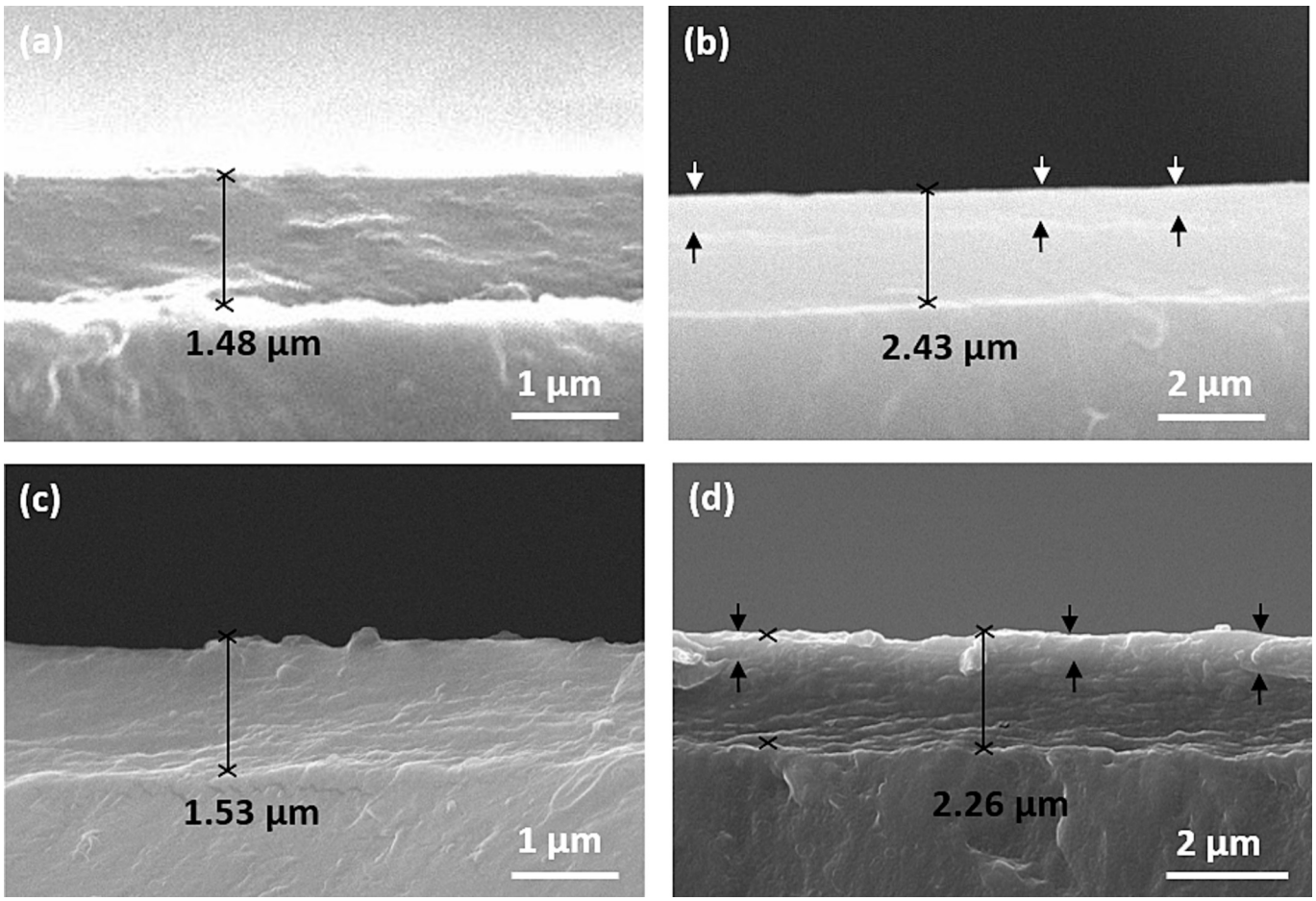

Fig. 5. Cross-sectional SEM images of CH/B/GO nanocomposite monolayer (a), CH/B/GO+CNC bilayer (b), CH/B/GO/CNC nanocomposite monolayer (c), and CH/B/GO+CNC/B/GO bilayer (d) coatings.

analysis, the filler concentration variation along the thickness of the coating is dramatically evident, with the formation of an extremely compact layer close to the surface, due to the strong interaction between CNCs and GO. This layer appears very dark due to the tight agglomeration of highly crystalline CNC and GO. (Fig. 6b). Furthermore, in the internal layer (Fig. 6c), graphene sheets are extremely oriented parallel to the substrate, maximizing the diffusion path of the permeants. This finding confirms what was previously observed by the authors, i.e. complete alignment of GO platelets in CH coating deposited with USS technique [10], and of CH films with GO/CNC hybrid filler and deposited by casting [19].

3.4. Gas barrier performance

The effect of the different structures and formulations on gas barrier performance of developed coatings was assessed by measuring the OTR of coated PBS films at 5% and 50% relative humidity. The results are reported as oxygen permeability (Fig. 7) to allow a better comparison of systems with different thicknesses. The oxygen permeability (OP) of PBS films, which was equal to $12.6 \pm 1.1 \times 10^{-15}$ cm^3 cm cm^{-2} s^{-1} Pa^{-1} at 5% RH, and $15.5 \pm 1.8 \times 10^{-15}$ cm^3 cm cm^{-2} s^{-1} Pa^{-1} at 50% RH, slightly decreased after the deposition of a 1.5 µm thick borax-crosslinked CH/GO coating (OP = $2.61 \pm 0.52 \times 10^{-15}$ cm^3 cm cm^{-2}

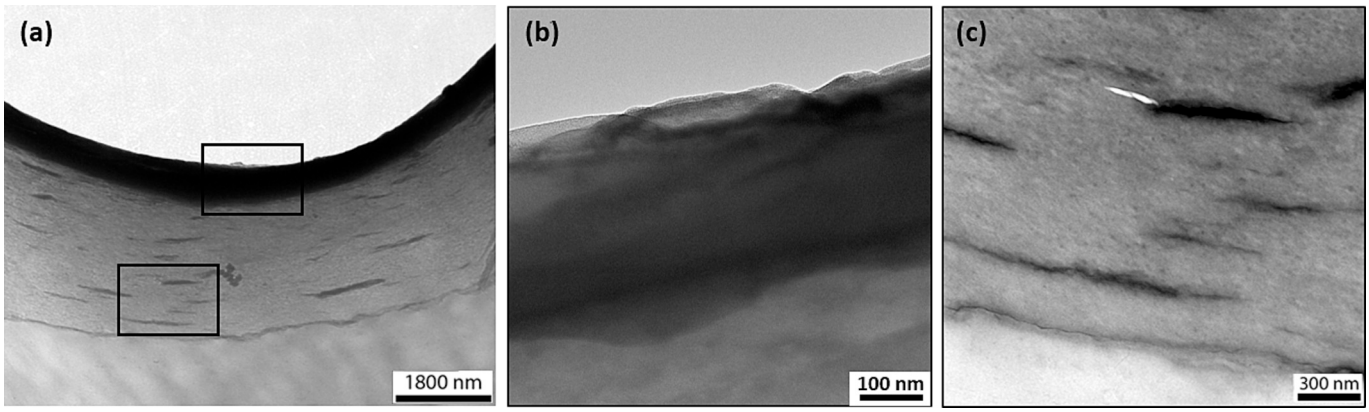

Fig. 6. Cross-sectional TEM images of CH/B/GO+CNC/B/GO bilayer coating at low (a) and high magnification (b,c).

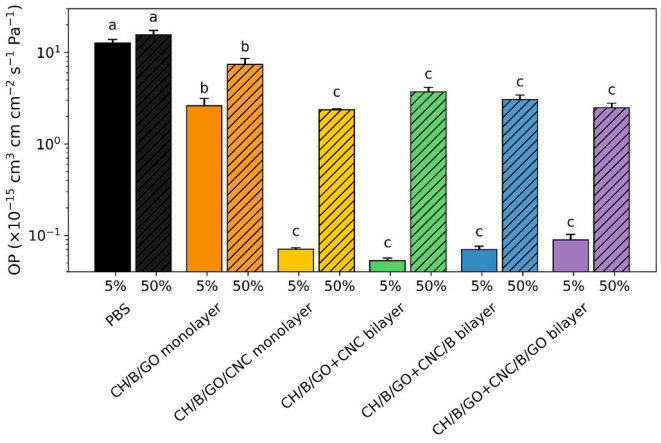

Fig. 7. Oxygen permeability of various coatings deposited on PBS films substrate.

s^{-1} Pa^{-1} at 5% RH, and 7.66 ± 1.12 × 10^{-15} cm^3 cm cm^{-2} s^{-1} Pa^{-1} at 50% RH). These results align with the OP values observed in the previous study of PEGDE-crosslinked CH/GO coatings with comparable thickness and 1 wt% GO [10]. The reduction is attributed to the presence of the GO nanoplatelet assembly, which significantly extends the diffusion path of the gas. On the other hand, the lower oxygen barrier with increasing humidity is due to the coating's hydrophilic nature, which causes the water molecules to plasticize the CH chains and expand the volume available for oxygen diffusion.

Cellulose nanocrystals were incorporated into the CH/B/GO coating formulation to improve the oxygen permeability (OP) by increasing the overall filler content while maintaining an effective nanofiller dispersion. Indeed, combining 1 wt% GO with 5 wt% CNC leads to a significant reduction in OP, with values of 0.070 ± 0.002 × 10^{-15} cm^3 cm cm^{-2} s^{-1} Pa^{-1} at 5% RH and 2.36 ± 0.06 × 10^{-15} cm^3 cm cm^{-2} s^{-1} Pa^{-1} at 50% RH. These numbers correspond to reductions of nearly three and one orders of magnitude, respectively, compared to uncoated PBS film. Moreover, the OP of CH/B/GO/CNC-coated films is significantly lower than that of CH/B/GO-coated films at 5% RH, and approximately 70% lower at 50% RH. This improvement in barrier performance can be attributed to the higher overall filler loading, as well as to borate ion crosslinking interactions with the hydroxyl groups of both CNC and GO, as also suggested by the zeta potential results (Section 3.1).

In a previous study we observed a deterioration of barrier properties with CH/GO coatings at GO loadings higher than 1 wt% [10], mainly due to platelet stacking and aggregation. In this context, the simultaneous dispersion of CNC and GO appears to be an effective strategy to overcome these limitations, as the zeta potential results demonstrated that the binary system showed enhanced colloidal stability. El Miri et al. and Jia et al. also investigated CNC/GO aqueous suspensions and corresponding films with varying filler ratios, demonstrating, via zeta potential and FTIR analyses, the presence of interfacial hydrogen bonding between the two components [18,46]. Furthermore, El Miri et al. observed through SEM and AFM analyses a homogeneous dispersion of CNC rods among GO sheets, forming a 3D interconnected network. The CNCs and GO interaction inhibits the sheet-to-sheet aggregation, thereby promoting a more uniform nanofiller distribution [18,49]. Thus, CNCs combination with the CH/GO formulation positively affect the nanocomposite characteristics that should be optimized to extend the gas diffusion path through a polymer matrix (i.e., nanofiller concentration and dispersion, structure density) [48].

The CH/B/GO+CNC/B/GO coatings exhibit a statistically comparable barrier performance to CH/B/GO/CNC under both RH conditions, showing an OP of 0.089 ± 0.012 × 10^{-15} cm^3·cm·cm^{-2}·s^{-1}·Pa^{-1} at 5% RH and 2.48 ± 0.29 × 10^{-15} cm^3·cm·cm^{-2}·s^{-1}·Pa^{-1} at 50% RH. Furthermore, the bilayer coatings prepared by depositing either pristine CNCs or borate-crosslinked CNCs as the surface barrier layer do not show statistically significant differences (CH/B/GO+CNC/B: OP = 0.071 ± 0.006 × 10^{-15} cm^3·cm·cm^{-2}·s^{-1}·Pa^{-1} at 5% RH and 3.04 ± 0.37 × 10^{-15} cm^3·cm·cm^{-2}·s^{-1}·Pa^{-1} at 50% RH; CH/B/GO+CNC: OP = 0.053 ± 0.003 × 10^{-15} cm^3·cm·cm^{-2}·s^{-1}·Pa^{-1} at 5% RH and 3.68 ± 0.44 × 10^{-15} cm^3·cm·cm^{-2}·s^{-1}·Pa^{-1} at 50% RH). However, a consistent decreasing trend in coating permeability is observed at 50% RH with increasing structural complexity of the upper layer in the bilayer systems, suggesting a potential contribution of borax crosslinking and GO platelets to barrier enhancement, although the differences are not statistically significant under the present experimental conditions.

The calculated OP values of the nanocomposite coatings, reported in Table S3, confirm that the CH/B/GO system exhibits significantly higher permeability compared to all CNC-containing coatings, while differences among CNC-based systems are less pronounced and not statistically significant. However, the lower standard deviation observed for the CH/B/GO/CNC nanocomposite monolayer suggests a higher coating homogeneity compared to the bilayer systems.

The measured permeability data of CH/B/GO and CH/B/CNC/GO nanocomposite monolayer, and CH/B/GO+CNC/B/GO bilayer under dry conditions were compared with the theoretical value predicted by the Cussler model (Fig. 8). The model correlates the gas permeability of nanocomposites (P) relative to the pristine polymer (P_0) with the nanoplatelet volume fraction (ϕ) and aspect ratio α, considering impermeable nanoplatelets distribute perpendicularly to the direction of the gas diffusion pathway through the entire polymer matrix. The relative permeability P/P_0, typically expressed as a function of the aspect ratio α and volume fraction ϕ of the GO nanoparticles, is described as:

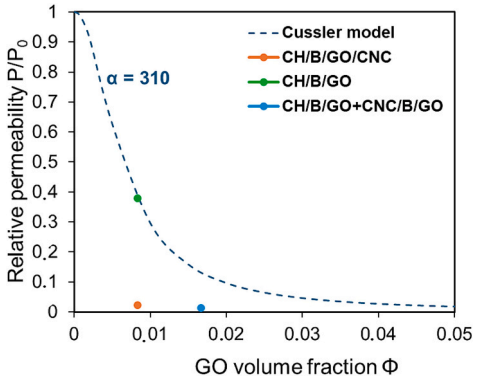

Fig. 8. Comparison between experimental relative oxygen permeability in dry conditions and the Cussler model for the relative permeability as a function of GO volume fraction.

$$\frac{P}{P^0} = \left(1 + \mu \frac{\alpha^2 \phi^2}{1 - \phi}\right) \quad (6)$$

where μ is the geometric factor which is assumed to be equal to 1. The theoretical aspect ratio of GO nanoplatelets was calculated by considering the permeability of the CH/B/GO under dry conditions as reference, and its GO volume fraction of 0.84% v/v. From Eq. (6), the obtained α value is 310, which is in good agreement with the value previously measured for this GO (α = 300) [22], further demonstrating the alignment of GO when deposited into CH solution by USS. However, the measured P/P₀ data for CH/B/GO/CNC and CH/B/GO+CNC/B/GO fall below those predicted by the 2D model proposed by Cussler in relation to their GO volume fraction. This deviation confirms that additional mechanisms are contributing to the reduced oxygen permeability in these coating architectures, most notably the effect of CNCs in densifying the barrier layer and the synergistic interactions between the two nanofillers.

The barrier performance observed in this work is consistent with literature reports on chitosan-based nanocomposite coatings. In previous work of the authors, multilayer nanocoatings incorporating chitosan and nanoplatelets such as GO and montmorillonite have been shown to reduce the OP of PET films by up to two orders of magnitude, both under dry and high humidity conditions [50]. On the other hand, Li et al. produced a 0.8 μm-thick multilayer CH/CNC coating, achieving a 94% reduction in the OP of PET films under dry conditions [51]. In this context, the system developed in the present work shows improved performance under low RH conditions. It should also be noted that the fabrication techniques adopted in the studies involve higher nanofiller loadings and require many deposition steps.

3.5. Water barrier performance

Fig. 9 shows the water vapor permeability of the developed coatings deposited on the PBS substrate. The variations to the coating design of the CH/GO nanocomposite system were aimed at reducing the hydrophilicity and water permeability. However, borax-crosslinked CH/GO nanocomposite deposition causes a worsening of the water vapor permeability of the PBS film, which turns from $2.74 \pm 0.10 \times 10^{-12}$ g cm cm^{-2} s^{-1} Pa^{-1} for bare PBS to $3.53 \pm 0.08 \times 10^{-12}$ g cm cm^{-2} s^{-1} Pa^{-1} for PBS coated with CH/B/GO. The coating layer swells significantly at high humidity due to the cleavage of hydrogen bonds and ionic interactions between CH chains or CH and GO, which opens up more diffusion paths. This increase is likely due to the greater hydrophilicity of the coating formulation compared to PBS, which increases the concentration gradient of water molecules along the coated film. Incorporating also 5 wt% CNCs in the CH/B/GO formulation decreases the WVP from $3.53 \pm 0.08 \times 10^{-12}$ g cm cm^{-2} s^{-1} Pa^{-1} to $2.37 \pm 0.08 \times 10^{-12}$ g cm cm^{-2} s^{-1} Pa^{-1}. Even though both GO and CNC are hydrophilic fillers, combining the two fillers benefits the water barrier. Consequently, the higher loading of dispersed nanofiller (6 wt% of total filler content) enhances the nanocomposite coating's water barrier.

The WVP of bilayer coatings with an upper layer of pristine CNC, borax-crosslinked CNC, and borax-crosslinked CNC containing 3 wt% GO was compared to better understand the effect of the surface layer. Applying a CNC layer over the CH/B/GO first layer does not affect water vapor permeability, yielding a WVP of $3.68 \pm 0.06 \times 10^{-12}$

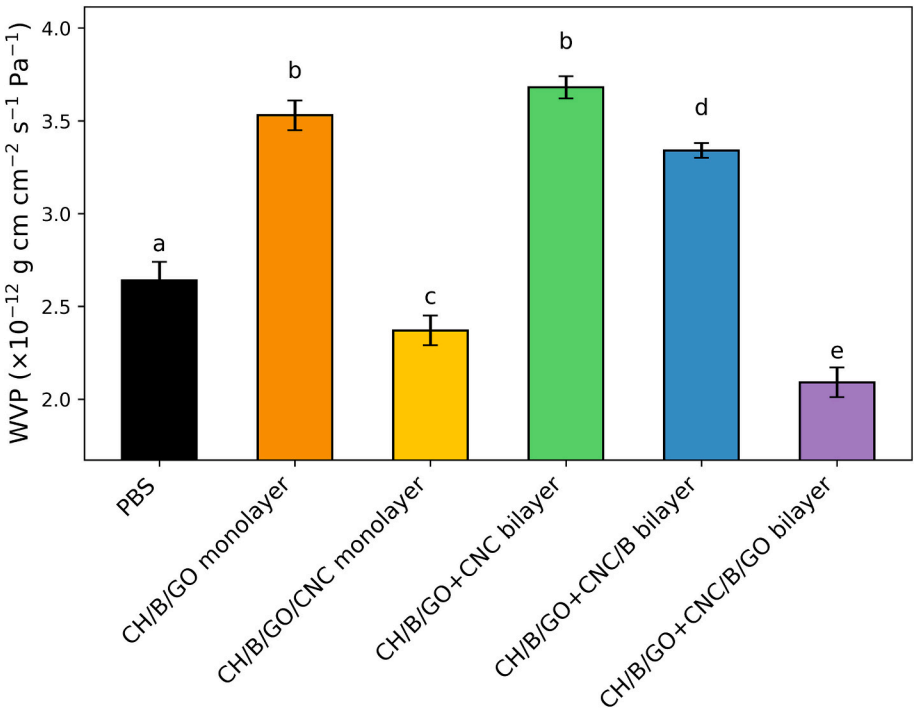

Fig. 9. Water vapor permeability of various coatings deposited on PBS substrate.

$g \cdot cm \cdot cm^{-2} \cdot s^{-1} \cdot Pa^{-1}$, as it is likely that only a fraction of the hydroxyl groups of the CNC rods interact with the underlying CH/B/GO layer, while the remaining groups are still available to interact with water molecules. In contrast, the deposition of an upper layer of borax-crosslinked CNCs decreases the WVP to $3.34 \pm 0.04 \times 10^{-12}$ g cm cm^{-2} s^{-1} Pa^{-1}. This moderate improvement in water vapor barrier performance can be attributed to crosslinking via borate–diol complexes, which reduce the number of free hydroxyl groups and decrease the accessible free volume for water diffusion. The CH/B/GO+CNC/B/GO system shows the lowest permeability, $2.09 \pm 0.08 \times 10^{-12}$ $g \cdot cm \cdot cm^{-2} \cdot s^{-1} \cdot Pa^{-1}$, suggesting that the combined effect of GO-induced tortuosity and borate crosslinking plays a key role in limiting water transport across the layer thickness.

The coating water permeability was also estimated using the ideal laminate theory (Table S4). The calculated values reflect the trends observed for the coated films. However, since water transport may involve additional effects such as polymer plasticization, swelling, and non-ideal interfacial behavior, these values should be considered as approximate estimations rather than intrinsic material properties.

Overall, the 1.5 μm thick CH/B/GO/CNC coating reduces the water vapor permeability of PBS by approximately 14%, while a 25% decrease is observed for the 2.2 μm thick CH/B/GO+CNC/B/GO bilayer coatings (based on average WVP values). Although the investigated strategies improve the water vapor barrier properties, the enhancement is significantly lower than that observed for oxygen barrier performance. This trend is also in line with literature reports on polysaccharide-based nanocomposite coatings. For instance, spray-coated bilayer coatings based on chitin nanowhiskers and cellulose nanocrystals have been shown to reduce oxygen permeability by up to 90–97%, while the corresponding reduction in water vapor permeability remains limited (typically around 20%) [52]. Similarly, chitosan/cellulose nanocrystal coatings deposited on paper substrates via slot-die coating exhibit significant improvements in oxygen barrier properties, whereas only moderate reductions in water vapor permeability are achieved [53]. This difference is attributed to the hydrophilic nature of natural polymers, e.g., CH and CNCs, as well as GO, which can readily absorb water molecules, leading to disruption of hydrogen bonding. Nevertheless, the investigated coating designs still provide a beneficial improvement in water vapor barrier properties.

3.6. Conclusions

In this study, sustainable gas and water barrier nanocomposite coatings, with a 1.5–2 μm thickness, were successfully fabricated using chitosan, CNCs, and GO, crosslinked with borax, following two different coating design strategies. The coatings were deposited onto compostable PBS films by ultrasonic spray coating, a simple, rapid, and easily scalable deposition technique suitable for industrial application. The water swelling resistance of the hydrophilic CH- and CNC-based coating formulations was significantly enhanced by the borax-crosslinked network linking CH with GO and CNC. The synergistic effect of the 1D filler (CNC) and the 2D filler (GO), either homogeneously dispersed within the chitosan matrix or anisotropically distributed along the coating thickness, led to a remarkable improvement in the oxygen permeability by almost 3 orders of magnitude at 5% RH, and by one order of magnitude at 50% RH. Likewise, the water vapor permeability of the PBS decreased by 14% with a 1.5-μm CH/B/GO/CNC nanocomposite monolayer and by 25% with a 2.2-μm CH/B/GO+CNC/B/GO bilayer, confirming that the anisotropic bilayer design more effectively suppresses water vapor permeation, although it requires higher filler content and longer processing, which may affect compostability and production cost.

This study shows how the type and distribution of fillers (CNC and GO) can be used to fine-tune nanocomposite barrier coatings, offering practical guidance for creating eco-friendly, high-performance films. Beyond scientific insight, the findings point toward real opportunities for sustainable packaging, especially for oxygen-sensitive products in humid conditions. Looking ahead, it will be important to explore comprehensive technological characterization, including adhesion and mechanical performance, long-term biodegradability, food-contact safety, and large-scale production to fully unlock the industrial potential of these coatings in view of practical packaging applications.

CRediT authorship contribution statement

Alessia Cabrini: Writing – original draft, Visualization, Methodology, Investigation, Formal analysis, Data curation, Conceptualization. **Hanieh Kargarzadeh:** Writing – review & editing, Investigation, Conceptualization. **Giovanna Giuliana Buonocore:** Methodology, Investigation. **Artur Różański:** Investigation. **Luigi De Nardo:** Writing – review & editing, Resources. **Gennaro Gentile:** Writing – review & editing, Validation, Methodology, Investigation. **Pierfrancesco Cerruti:** Writing – review & editing, Supervision, Resources, Project administration. **Marino Lavorgna:** Writing – review & editing, Supervision, Resources, Conceptualization.

Declaration of competing interest

The authors declare that they have no known competing financial interests or personal relationships that could have appeared to influence the work reported in this paper.

Acknowledgment

This work was financially supported by PRIN2022 BAC4PACK project (CUP B53D23008880006), the National Key Research and Development Program of China (2023YFE0105600) “Joint Laboratory on Multifunctional Polymer Nanocomposites based on Graphene Related Materials”, and the European Union Next GenerationEU (PIANO NAZIONALE DI RIPRESA E RESILIENZA (PNRR) within the following project: MICS (Made in Italy – Circular and Sustainable) Extended Partnership (PNRR-MISSIONE 4 COMPONENTE 2, INVESTIMENTO 1.3 – D.D. 1551.11-10-2022, PE00000004).

Appendix A. Supplementary data

Supplementary data to this article can be found online at https://doi.org/10.1016/j.porgcoat.2026.110190.

Data availability

No data was used for the research described in the article.

References

[1] Y. Liu, et al., A review of cellulose and its derivatives in biopolymer-based for food packaging application, Trends Food Sci. Technol. 112 (2020) (2021) 532–546, https://doi.org/10.1016/j.tifs.2021.04.016.
[2] S. Khan, L. Lorenzelli, R.S. Dahiya, Technologies for printing sensors and electronics over large flexible substrates: a review, IEEE Sensors J. 15 (6) (2015) 3164–3185, https://doi.org/10.1109/JSEN.2014.2375203.
[3] Z. Zhang, I.J. Britt, M.A. Tung, Permeation of oxygen and water vapor through EVOH films as influenced by relative humidity, J. Appl. Polym. Sci. 82 (8) (2001) 1866–1872, https://doi.org/10.1002/app.2030.
[4] M. Brochhagen, S. Chur, V. Layes, M. Böke, J. Benedikt, Deposition of SiOx coatings by inductively coupled plasma: effect of pulsed hexamethyldisiloxan flow, Plasma Process. Polym. 15 (4) (2018) 1–11, https://doi.org/10.1002/ppap.201700186.
[5] M. Mujtaba, J. Lipponen, M. Ojanen, S. Puttonen, H. Vaittinen, Trends and challenges in the development of bio-based barrier coating materials for paper/cardboard food packaging; a review, Sci. Total Environ. 851, no. June (2022) 158328, https://doi.org/10.1016/j.scitotenv.2022.158328.
[6] M. Flórez, E. Guerra-Rodríguez, P. Cazón, M. Vázquez, Chitosan for food packaging: recent advances in active and intelligent films, Food Hydrocoll. 124 (2022), https://doi.org/10.1016/j.foodhyd.2021.107328.

[7] I.S. Bayer, Superhydrophobic coatings from ecofriendly materials and processes: a review, Adv. Mater. Interfaces 7 (13) (2020) 1–25, https://doi.org/10.1002/admi.202000095.
[8] V. Siracusa, P. Rocculi, S. Romani, M.D. Rosa, Biodegradable polymers for food packaging: a review, Trends Food Sci. Technol. 19 (12) (2008) 634–643, https://doi.org/10.1016/j.tifs.2008.07.003.
[9] Y. Cui, S.I. Kundalwal, S. Kumar, Gas barrier performance of graphene/polymer nanocomposites, Carbon N. Y. 98 (2016) 313–333, https://doi.org/10.1016/j.carbon.2015.11.018.
[10] A. Cabrini, et al., Ultrasonic spray deposition of PEGDE-crosslinked chitosan/graphene oxide coatings for enhancing gas barrier properties of polybutylene succinate films, Prog. Org. Coat. 183 (May) (2023), https://doi.org/10.1016/j.porgcoat.2023.107760.
[11] C. Gómez H., et al., Vegetable nanocellulose in food science: a review, Food Hydrocoll. 57 (2016) 178–186, https://doi.org/10.1016/j.foodhyd.2016.01.023.
[12] G. Tedeschi, et al., Sustainable, high-barrier polyaleuritate/nanocellulose biocomposites, ACS Sustain. Chem. Eng. 8 (29) (2020) 10682–10690, https://doi.org/10.1021/acssuschemeng.0c00909.
[13] V.G.L. Souza, J.R.A. Pires, C. Rodrigues, I.M. Coelhoso, A.L. Fernando, Chitosan composites in packaging industry-current trends and future challenges, Polymers (Basel) 12 (2) (2020) 1–16, https://doi.org/10.3390/polym12020417.
[14] M.H. Salim, Y. Abdellaoui, A. Ait Benhamou, E.H. Ablouh, M. El Achaby, Z. Kassab, Influence of cellulose nanocrystals from pea pod waste on mechanical, thermal, biodegradability, and barrier properties of chitosan-based films, Cellulose 29 (9) (2022) 5117–5135, https://doi.org/10.1007/s10570-022-04587-6.
[15] M. Yadav, K. Behera, Y.H. Chang, F.C. Chiu, Cellulose nanocrystal reinforced chitosan based UV barrier composite films for sustainable packaging, Polymers (Basel) 12 (1) (2020), https://doi.org/10.3390/polym12010202.
[16] H.M.C. Azeredo, et al., Nanocellulose reinforced chitosan composite films as affected by nanofiller loading and plasticizer content, J. Food Sci. 75 (1) (2010) 1–7, https://doi.org/10.1111/j.1750-3841.2009.01386.x.
[17] F.A. Corsello, P.A. Bolla, P.S. Anbinder, M.A. Serradell, J.I. Amalvy, P.J. Peruzzo, Morphology and properties of neutralized chitosan-cellulose nanocrystals biocomposite films, Carbohydr. Polym. 156 (2017) 452–459, https://doi.org/10.1016/j.carbpol.2016.09.031.
[18] N. El Miri, et al., Synergistic effect of cellulose nanocrystals/graphene oxide nanosheets as functional hybrid nanofiller for enhancing properties of PVA nanocomposites, Carbohydr. Polym. 137 (2016) 239–248, https://doi.org/10.1016/j.carbpol.2015.10.072.
[19] C. Santillo, et al., Hybrid graphenene oxide/cellulose nanofillers to enhance mechanical and barrier properties of chitosan-based composites, Front. Chem. 10 (July) (2022) 1–13, https://doi.org/10.3389/fchem.2022.926364.
[20] B. Wicklein, D. Kocjan, F. Carosio, G. Camino, L. Bergström, Tuning the nanocellulose-borate interaction to achieve highly flame retardant hybrid materials, Chem. Mater. 28 (7) (2016) 1985–1989, https://doi.org/10.1021/acs.chemmater.6b00564.
[21] C.L. Lai, et al., Bio-inspired cross-linking with borate for enhancing gas-barrier properties of poly(vinyl alcohol)/graphene oxide composite films, Carbon N. Y. 82 (C) (2015) 513–522, https://doi.org/10.1016/j.carbon.2014.11.003.
[22] N. Yan, et al., Borate cross-linked graphene oxide-chitosan as robust and high gas barrier films, Nanoscale 8 (20) (2016) 10783–10791, https://doi.org/10.1039/c6nr00377j.
[23] S. Qin, et al., Super gas barrier and fire resistance of nanoplatelet/nanofibril multilayer thin films, Adv. Mater. Interfaces 6 (2) (2019) 1–6, https://doi.org/10.1002/admi.201801424.
[24] F. Ren, et al., Ultra-low gas permeable cellulose nano fiber nanocomposite films filled with highly oriented graphene oxide nanosheets induced by shear field 209 (January) (2019) 310–319, https://doi.org/10.1016/j.carbpol.2019.01.040.
[25] W.S. Hummers, R.E. Offeman, Preparation of graphitic oxide, J. Am. Chem. Soc. 80 (6) (1958) 1339, https://doi.org/10.1021/ja01539a017.
[26] D. Bondeson, A. Mathew, K. Oksman, Optimization of the isolation of nanocrystals from microcrystalline cellulose by acid hydrolysis, Cellulose 13 (2) (2006) 171–180, https://doi.org/10.1007/s10570-006-9061-4.
[27] M. Rietjens, P.A. Steenbergen, Crosslinking mechanism of boric acid with diols revisited, Eur. J. Inorg. Chem. 6 (2005) 1162–1174, https://doi.org/10.1002/ejic.200400674.
[28] J.A. Peters, Interactions between boric acid derivatives and saccharides in aqueous media: structures and stabilities of resulting esters, Coord. Chem. Rev. 268 (2014) 1–22, https://doi.org/10.1016/j.ccr.2014.01.016.
[29] H. Lundberg, F. Tinnis, N. Selander, H. Adolfsson, Catalytic amide formation from non-activated carboxylic acids and amines, Chem. Soc. Rev. 43 (8) (2014) 2714–2742, https://doi.org/10.1039/c3cs60345h.
[30] S. Tanpichai, F. Phoothong, A. Boonmahitthisud, Superabsorbent cellulose-based hydrogels cross-liked with borax, Sci. Rep. 12 (1) (2022) 1–12, https://doi.org/10.1038/s41598-022-12688-2.
[31] S. Jabeen, S. Saeed, A. Kausar, B. Muhammad, S. Gul, M. Farooq, Influence of chitosan and epoxy cross-linking on physical properties of binary blends, Int. J. Polym. Anal. Charact. 21 (2) (2016) 163–174, https://doi.org/10.1080/1023666X.2016.1131404.
[32] B. Kaya, N.N. Zorba, C. Caner, Development of novel biodegradable film based on chitosan with borax (sodium tetraborate) and boron nitride and their biological activity, Int. J. Food Sci. Technol. 58 (2) (2023) 890–897, https://doi.org/10.1111/ijfs.15743.
[33] W. Ge, S. Cao, F. Shen, Y. Wang, J. Ren, X. Wang, Rapid self-healing, stretchable, moldable, antioxidant and antibacterial tannic acid-cellulose nanofibril composite hydrogels, Carbohydr. Polym. 224 (June) (2019) 115147, https://doi.org/10.1016/j.carbpol.2019.115147.
[34] K. Sahlin, L. Forsgren, T. Moberg, D. Bernin, M. Rigdahl, G. Westman, Surface treatment of cellulose nanocrystals (CNC): effects on dispersion rheology, Cellulose 25 (1) (2018) 331–345, https://doi.org/10.1007/s10570-017-1582-5.
[35] S. Sheikh, M. Rahman, S. Rahman, K. Yildirim, Fabrication of nano composite membrane filter from graphene oxide (GO) and banana rachis cellulose nano crystal (CNC) for industrial effluent treatment, J. Ind. Eng. Chem. 128 (2023) 196–208, https://doi.org/10.1016/j.jiec.2023.07.048.
[36] H.D. Ozcan Koysuren, Mustafa Karaman, Preparation and characterization of Polyvinyl Borate/Polyvinyl Alcohol (PVB/PVA) blend nanofibers, J. Appl. Polym. Sci. 124 (2012) 2736–2741.
[37] K. Yoshimura, Y. Miyazaki, F. Ota, S. Matsuoka, H. Sakashita, Complexation of boric acid with the N-methyl-D-glucamine group in solution and in crosslinked polymer, J. Chem. Soc. Faraday Trans. 94 (5) (1998) 683–689, https://doi.org/10.1039/a707790d.
[38] T. Itou, H. Kitai, A. Shimazu, T. Miyazaki, K. Tashiro, Clarification of cross-linkage structure in boric acid doped poly(vinyl alcohol) and its model compound as studied by an organized combination of x-ray single-crystal structure analysis, raman spectroscopy, and density functional theoretical calculation, J. Phys. Chem. B 118 (22) (2014) 6032–6037, https://doi.org/10.1021/jp5026569.
[39] L. Bonetti, L. De Nardo, L. De Nardo, F. Variola, S. Fare', S. Fare', Evaluation of the subtle trade-off between physical stability and thermo-responsiveness in crosslinked methylcellulose hydrogels, Soft Matter 16 (24) (2020) 5577–5587, https://doi.org/10.1039/d0sm00269k.
[40] C. Li, et al., Synthesis, characterizations, and release mechanisms of carboxymethyl chitosan-graphene oxide-gelatin composite hydrogel for controlled delivery of drug, Inorg. Chem. Commun. 155 (2023) 110965, https://doi.org/10.1016/j.inoche.2023.110965.
[41] N. El Miri, et al., Synergistic effect of cellulose nanocrystals/graphene oxide nanosheets as functional hybrid nanofiller for enhancing properties of PVA nanocomposites, Carbohydr. Polym. 137 (2016) 239–248, https://doi.org/10.1016/j.carbpol.2015.10.072.
[42] M.Z. Khajavi, A. Ebrahimi, M. Yousefi, S. Ahmadi, M. Farhoodi, Strategies for Producing Improved Oxygen Barrier Materials Appropriate for the Food Packaging Sector, 2020, pp. 346–363.
[43] S. Bose, S.S. Keller, A. Boisen, Process optimization of ultrasonic spray coating of polymer films, Langmuir (2013), https://doi.org/10.1021/la4010246.
[44] M. Abbas, M. Buntinx, W. Deferme, N. Reddy, R. Peeters, Oxygen gas and uv barrier properties of nano-ZnO-coated pet and phbhhx materials fabricated by ultrasonic spray-coating technique, Nanomaterials 11 (2) (2021) 1–14, https://doi.org/10.3390/nano11020449.
[45] J.S. Bunch, et al., Impermeable Atomic Membranes From 2008, 2008, pp. 3–7.
[46] J. Li, J.A. Viveros, M.H. Wrue, M. Anthamatten, A self-healing gel from borax and polymer precursors, Macromolecules 45 (15) (2012) 6334–6340.
[47] Y. Liu, Z. Cai, L. Sheng, M. Ma, Q. Xu, Y. Jin, Structure-property of crosslinked chitosan/silica composite films modified by genipin and glutaraldehyde under alkaline conditions, Carbohydr. Polym. 215 (348–357) (2019) 0144–8617, https://doi.org/10.1016/j.carbpol.2019.04.001.
[48] Y. Jia, C. Hu, P. Shi, Q. Xu, W. Zhu, R. Liu, Effects of cellulose nanofibrils/graphene oxide hybrid nanofiller in PVA nanocomposites, Int. J. Biol. Macromol. 161 (2020) 223–230, https://doi.org/10.1016/j.ijbiomac.2020.06.013.
[49] W. Fan, J. Wang, Z. Zhang, Z. Li, Synergistic enhancement of UV resistance and electrical conductivity of waterborne polyurethane composite with combination of functionalized 2D graphene oxide and 1D nanocellulose, Prog. Org. Coat. 151 (2021) 106017, https://doi.org/10.1016/j. porg. coat.2020.
[50] A. Cabrini, S.G. Fisher, E.T. Iverson, P. Cerruti, L. De Nardo, G. Gentile, M. Lavorgna, J.C. Grunlan, High gas barrier of clay/graphene oxide/chitosan multilayer nanocoatings at high humidity, Prog. Org. Coat. 198 (2025) 108929.
[51] F. Li, P. Biagioni, M. Finazzi, S. Tavazzi, L. Piergiovanni, Tunable green oxygen barrier through layer-by-layer self-assembly of chitosan and cellulose nanocrystals, Carbohydr. Polym. 92 (2) (2013) 2128–2134.
[52] Y. Ji, S. Waters, E. Lim, A.W. Lang, P.N. Ciesielski, M.L. Shofner, J.R. Reynolds, J. C. Meredith, Minimizing oxygen permeability in chitin/cellulose nanomaterial coatings by tuning chitin deacetylation, ACS Sustain. Chem. Eng. 10 (1) (2022) 124–133, https://doi.org/10.1021/acssuschemeng.1c05051.
[53] Y. Ruberto, V. Vivod, J.J. Grkman, et al., Slot-die coating of cellulose nanocrystals and chitosan for improved barrier properties of paper, Cellulose 31 (2024) 3589–3606, https://doi.org/10.1007/s10570-024-05847-3.